Journal of Physics and Its Applications

Journal homepage : https://ejournal2.undip.ac.id/index.php/jpa/index

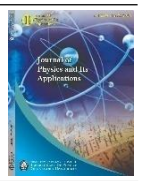

Composition-Dependent Structural and Dynamical Properties of Mixed DPPC/DLPC Bilayers: An Atomistic Molecular Dynamics Study

Gregoria Illya[1*] and Hadi Sutanto[2]

[1]*Department of Physics, Faculty of Mathematics and Natural Sciences, Matana University, Tangerang, Indonesia*
[2]*Department of Mechanical Engineering, Atma Jaya Catholic University of Indonesia, Jakarta, Indonesia*

**Corresponding author: gregoria.illya@matanauniversity.ac.id*

A R T I C L E I N F O

Article history:
Received: 28 February 2026
Accepted: 03 August 2026
Available online: 31 August 2026

Keywords:
Molecular dynamics simulation
Phospholipid mixture
Biological membrane
Lipid interdigitation
Hydrophobic mismatch

ABSTRACT

Moderate chain-length mismatch in saturated lipid mixtures provides a useful model for understanding how structural perturbations influence membrane behavior. Here, all-atom molecular dynamics simulations were used to investigate DPPC/DLPC bilayers across compositions at 50 °C, focusing on the coupled evolution of structure, dynamics, and hydration. Increasing DLPC content leads to a systematic increase in area per lipid and a reduction in bilayer thickness, indicating weakened packing within the hydrophobic core. These structural changes are accompanied by enhanced interleaflet coupling and decreased acyl-chain ordering. The lateral diffusion behavior is composition-dependent: DLPC mobility increases steadily with concentration, whereas DPPC exhibits a non-monotonic trend, reflecting competing effects of increased free volume and heterogeneous packing. Mean squared displacement analysis in log–log representation reveals persistent subdiffusive dynamics for both lipid species, with diffusion exponents $\alpha \approx 0.30–0.35$ across all compositions. This indicates that lipid motion remains governed by transient confinement and spatial heterogeneity, even as overall mobility increases. In parallel, water density profiles show enhanced penetration of water into the bilayer interior with increasing DLPC fraction, driven by packing defects and increased free volume rather than pore formation. These results demonstrate that moderate chain-length mismatch induces a coupled structural and dynamical response that governs membrane transport properties.

1. Introduction

Biological membranes are dynamic, multicomponent assemblies whose physical properties are governed by lipid composition. Variations in acyl-chain length, saturation, and headgroup chemistry regulate membrane packing, thickness, elasticity, and permeability. In particular, differences in hydrocarbon chain length introduce hydrophobic mismatch, which perturbs bilayer structure by modifying thickness, chain ordering, and interleaflet interactions [1–6]. In mixed lipid systems, incorporation of shorter acyl chains weakens van der Waals interactions and increases free volume, leading to bilayer thinning and reduced packing efficiency [4–8].

While these structural effects are well established, their implications for lipid transport and membrane hydration remain incompletely understood. Most prior studies have focused on equilibrium structural descriptors or on systems involving unsaturated lipids and coarse-grained models, leaving a limited atomistic picture of how chain-length asymmetry in saturated phosphatidylcholines governs lipid mobility, interleaflet coupling, and water distribution. In particular, it is still unclear whether increased membrane fluidity under such conditions results in conventional Fickian diffusion or retains signatures of anomalous, subdiffusive dynamics.

Molecular dynamics (MD) simulations provide a powerful framework to address these questions at atomistic resolution. By enabling direct analysis of spatially resolved density distributions, lipid packing, and transport behavior, MD has become an essential tool for quantifying key membrane properties such as area per lipid, bilayer thickness, electron density profiles, and diffusion coefficients [1,9–11]. Establishing clear relationships between composition, structure, and transport is also critical for applications such as liposomal drug delivery, where membrane fluidity and permeability must be carefully balanced to optimize stability and release behavior [12, 13].

In this work, we perform all-atom MD simulations of DPPC/DLPC bilayers across a range of compositions at 50 °C. To the best of our knowledge, a systematic atomistic characterization of this binary saturated phosphatidylcholine system, combining structural, dynamical, and hydration analyses within a single framework, has not been reported. By integrating metrics such as area per lipid, bilayer thickness, density profiles, interleaflet coupling, lateral diffusion, and the anomalous diffusion exponent (α), we demonstrate that increasing DLPC fraction induces bilayer thinning, chain disorder, and enhanced interleaflet coupling, while lipid motion remains subdiffusive across all compositions. These results establish a direct link between hydrophobic

mismatch, heterogeneous dynamics, and membrane hydration, providing new insight into the molecular mechanisms governing transport and stability in lipid membranes.

2. Methodology

2.1. Simulation Setup

Binary mixed bilayers composed of 1,2-dipalmitoyl-sn-glycero-3-phosphocholine (DPPC) and 1,2-dilauroyl-sn-glycero-3-phosphocholine (DLPC) lipids at several molar ratios (75:25 ($\pi = 0.25$), 50:50 ($\pi = 0.50$), and 25:75 ($\pi = 0.75$)) were investigated.

The initial structures of the all-atom (AA) bilayer systems were generated using the heterogeneous lipid builder in the Membrane Builder module of CHARMM-GUI [14–16]. Each system contained 100 lipids per leaflet arranged in a rectangular simulation box and hydrated with 2.25-nm-thick water layers above and below the bilayer.

The bilayer area in the x–y plane was approximately 8 × 8 nm^2, corresponding to an area per lipid of about 60–65 $Å^2$. The ionic strength was set to 150 mM (0.15 $mol \cdot L^{-1}$) by adding sodium chloride to mimic physiological serum conditions. The CHARMM36 force field [17–19] was employed to model lipids and ions, while water molecules were represented using the TIP3P model [20]. During equilibration, positional restraints on the lipids were gradually reduced over a total equilibration time of 2.25 ns.

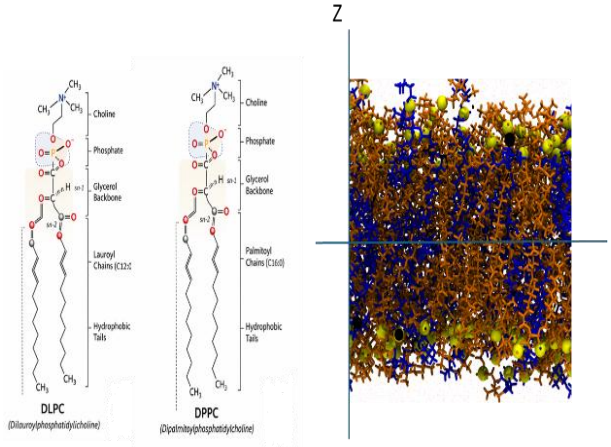

Fig. 1: Molecular structures of DLPC and DPPC and representative snapshot of the mixed bilayer

Fig. 1 presents the molecular structures of DLPC and DPPC together with a representative snapshot of the mixed bilayer. The chemical structures highlight that dilauroylphosphatidylcholine (DLPC, C12:0) and dipalmitoylphosphatidylcholine (DPPC, C16:0) share identical phosphatidylcholine headgroups but differ in their acyl-chain lengths. The accompanying molecular dynamics snapshot illustrates the organization of the mixed DPPC/DLPC bilayer, where DPPC tails are shown in blue and DLPC tails in orange, while yellow spheres denote the phosphate headgroup atoms. The bilayer is centered at $z = 0$, corresponding to the membrane midplane.

2.2. Simulation Parameters

All all-atom (AA) molecular dynamics (MD) simulations were performed using the GROMACS (v2025.0) simulation package [21–23]. Following the standard six-step CHARMM-GUI equilibration protocol, each system was further equilibrated for 150 ns using a 2 fs integration time step. Production simulations were subsequently carried out for 300 ns.

Temperature was maintained at T = 323.15 K using the velocity-rescale (v-rescale) thermostat [24] with separate coupling groups for the membrane (MEMB) and solvent (SOLV), each with a coupling constant of 1.0 ps. Pressure was controlled semi-isotropically using the Parrinello–Rahman barostat with a reference pressure of 1 bar, a time constant of 12.0 ps, and a compressibility of 4.5×10^{-5} bar^{-1} [25].

Short-range van der Waals interactions were treated using a force-switch cutoff between 1.0 and 1.2 nm, while long-range electrostatics were computed using the particle mesh Ewald (PME) method with a real-space cutoff of 1.2 nm [26]. All bonds involving hydrogen atoms were constrained using the LINCS algorithm, allowing a 2 fs time step [27].

Periodic boundary conditions were applied in all directions, and dispersion corrections were included for both energy and pressure.

2.3. Simulation Analysis

2.3.1. Area per Lipid and Bilayer Thickness

The average area per lipid (APL), also referred to as the headgroup area, was calculated by dividing the instantaneous lateral box area (Lx × Ly) by the number of lipids in a single leaflet and subsequently averaging over the production trajectory. This quantity provides a measure of the lateral packing density of the membrane.

The bilayer thickness was determined from the average separation between the two leaflets. Specifically, the mean z-coordinates of the phosphorus (P) atoms in the upper and lower leaflets were computed for each frame, and the thickness was obtained from the difference between these two averaged positions. Time averaging over the equilibrated trajectory yielded the reported thickness values. It should be noted that the bilayer thickness is influenced by the extent of interleaflet penetration and chain interdigitation, which can modify the effective separation between the opposing leaflets in mixed lipid systems.

2.3.2. Tail Mass and Electron Density Profiles

Density profiles along the bilayer normal (z-axis) were calculated to characterize the transverse membrane structure. For each trajectory frame, the bilayer was first centered using the center of mass of all lipid atoms to remove translational drift. The simulation box was then divided into thin slabs along the z direction.

The tail mass density profile was obtained by accumulating the atomic masses of the lipid acyl-chain atoms (sn-1 and sn-2 hydrocarbon tails) within each slab. The resulting profiles were normalized to their maximum values to facilitate comparison

between systems and to probe possible interdigitation within the hydrophobic core.

In parallel, the electron density profile of the lipids was computed using all lipid atoms by summing their atomic electron numbers within each slab and applying the same normalization procedure. Species-resolved profiles were generated separately for DPPC and DLPC to examine compositional effects.

All density profiles were averaged over the equilibrated portion of the production trajectory. The symmetry of the resulting profiles about the bilayer midplane was used as an additional indicator of proper equilibration and leaflet balance.

2.3.3. Interleaflet Coupling Analysis

Interleaflet coupling arising from hydrophobic mismatch was quantified using the chain overlap coefficient, d_{overlap}, which characterizes the effective extension of lipid acyl chains relative to the bilayer thickness. The coefficient is defined as

$$d_{overlap} = \frac{2l_z - d_c}{l_z} \quad (1)$$

where d_c represents the thickness of the hydrophobic core and l_z is the average projected length of the lipid acyl chains along the bilayer normal (z-axis).

The projected chain length was calculated as

$$l_z = |\langle z_s \rangle - \langle z_t \rangle| \quad (2)$$

where $\langle z_s \rangle$ and $\langle z_t \rangle$ denote the time-averaged z-coordinates of the initial and terminal carbon atoms of the acyl chains, respectively [4].

For each composition, d_{overlap} was computed and averaged over the equilibrated portion of the trajectory. Although commonly associated with interdigitation, this parameter depends on the projected chain length and therefore reflects the combined effects of chain orientation, conformational disorder, and interleaflet interactions. In this work, d_{overlap} is interpreted as a measure of effective interleaflet coupling rather than a direct measure of geometric chain interpenetration.

2.3.4. Acyl Chain Order Parameters

The conformational ordering of the lipid acyl chains was quantified using the deuterium order parameter, S_{CD}. For each methylene segment along the sn-1 and sn-2 chains, S_{CD} was calculated from the time-averaged orientation of the C–H bonds relative to the bilayer normal (z-axis):

$$|S_{CD}| = \frac{1}{2}\langle 3\cos^2\theta - 1 \rangle \quad (3)$$

where θ is the angle between the C–H bond vector and the bilayer normal [8]. The order parameters were computed separately for DPPC and DLPC and averaged over lipids and over the equilibrated trajectory. The resulting profiles provide insight into chain packing and conformational disorder as a function of lipid composition.

2.3.5. Lateral Diffusion Analysis

Lateral diffusion of lipids within the membrane plane was characterized using the mean squared displacement (MSD) of the lipid center of mass projected onto the xy plane. The MSD was calculated as a function of lag time and averaged over all lipids of each species.

The lateral diffusion coefficient D was obtained from the long-time regime of the MSD using the two-dimensional Einstein relation:

$$MSD(t) = 4Dt \quad (4)$$

where t is the time interval. The fitting was restricted to the long-time region to ensure consistent comparison of diffusion coefficients across compositions.

To further characterize the nature of lipid transport, the MSD was analyzed in log–log representation to determine the anomalous diffusion exponent α, defined by

$$MSD(t) \propto t^{\alpha} \quad (5)$$

The exponent α was obtained by fitting the MSD over the time interval of 5–30 ns, where the scaling behavior was stable. Values of $\alpha = 1$ correspond to normal Fickian diffusion, whereas $\alpha < 1$ indicates subdiffusive motion arising from transient confinement and heterogeneous membrane environments.

Both the diffusion coefficient D and the exponent α were determined separately for DPPC and DLPC at each composition to capture species-specific differences in lipid mobility and transport behavior.

2.3.6. Water Density and Penetration Analysis

Water penetration into the bilayer was quantified from the number density profile of water oxygen atoms along the bilayer normal (z-axis). For each trajectory frame, the bilayer was recentered using the center of mass of all lipid atoms to remove translational drift. The simulation box was divided into thin slabs within a ±6 nm window, and the spatial distribution of water oxygen atoms was accumulated and normalized by the corresponding slab volume to obtain the water number density.

In addition, the integrated water content within the hydrophobic core was calculated by numerically integrating the water density over the central core region ($|z| \leq 1.0$ nm), providing a quantitative measure of the total amount of water present inside the membrane interior.

3. Results and Discussion

3.1. Area per Lipid and Bilayer Thickness

The average area per lipid (APL) increases monotonically with DLPC mole fraction (Fig. 2). Specifically, the APL rises from 60.81 ± 0.14 Å^2 at π = 0.25 to 62.59 ± 0.14 Å^2 at π = 0.50 and further to 62.93 ± 0.04 Å^2 at π = 0.75. This nearly linear dependence indicates a progressive lateral expansion of the membrane as the fraction of the shorter DLPC lipid increases.

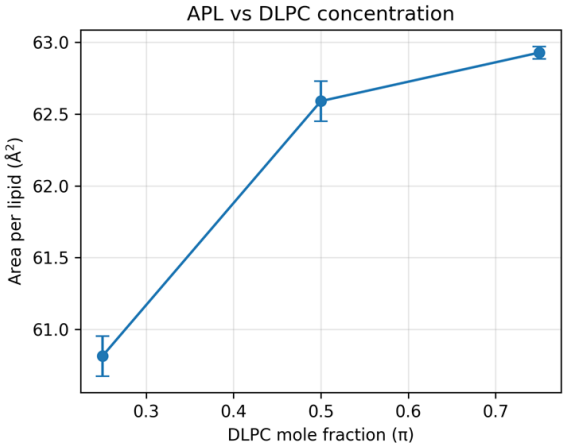

Fig. 2: Area per lipid versus DLPC mole fraction in DPPC/DLPC bilayers at 50 °C

This trend reflects the reduced hydrocarbon chain length of DLPC compared to DPPC. The shorter C12 chains weaken van der Waals interactions within the hydrophobic core, leading to less efficient packing and an increase in the effective lateral area per molecule. Importantly, this expansion is not merely a geometric effect but reflects a reduction in cohesive interactions between lipid tails, which enhances local free volume and promotes configurational flexibility. Similar behavior has been reported in mixed bilayers, where increasing the fraction of shorter lipids leads to expansion of the headgroup area due to reduced packing constraints and increased steric repulsion [4, 8, 28].

The absolute APL values obtained here fall within the expected range for fluid-phase phosphatidylcholine membranes. Experimental and simulation studies typically report APL values of approximately 62–64 Å² for pure DPPC in the L_α phase near 50 °C [28–30], while shorter-chain PCs such as DLPC exhibit slightly larger molecular areas. The agreement with literature values supports the reliability of the simulation setup and equilibration protocol.

Consistent with the lateral expansion, the bilayer thickness, determined from the phosphate–phosphate separation, decreases systematically with increasing DLPC content (Fig. 3). The thickness reduces from 3.740 ± 0.007 nm at π = 0.25 to 3.484 ± 0.006 nm at π = 0.50 and further to 3.294 ± 0.002 nm at π = 0.75. These values are consistent with reported thicknesses for fluid phosphatidylcholine bilayers, where DPPC typically exhibits values in the range of 3.6–3.9 nm depending on temperature and methodology [31].

The simultaneous increase in area per lipid and decrease in bilayer thickness reflects a reduction in packing efficiency associated with the incorporation of shorter DLPC chains. This trend signifies a redistribution of molecular packing within the bilayer, where looser lateral organization is accompanied by a thinner hydrophobic core. As a result, lipid chains from opposing leaflets can approach more closely, leading to enhanced interleaflet coupling. Similar coupling between increased area per lipid and reduced thickness has been reported in mixed systems with chain-length asymmetry [4].

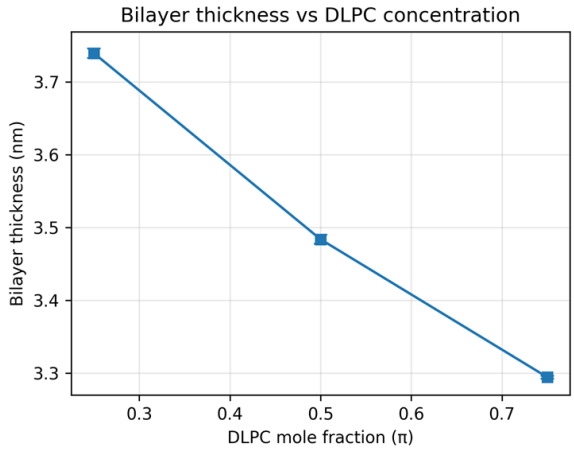

Fig. 3: Bilayer thickness versus DLPC mole fraction in DPPC/DLPC bilayers at 50 °C

Overall, increasing DLPC fraction induces a coordinated structural rearrangement characterized by reduced packing density, increased free volume, and bilayer thinning. These changes provide the structural basis for the heterogeneous dynamics and enhanced hydration discussed in the following sections.

3.2. Tail Mass Density and Electron Density Profiles

The transverse organization of the mixed DPPC/DLPC bilayers was analyzed using species-resolved acyl-chain (tail) mass density profiles and electron density distributions along the bilayer normal.

The tail density profiles (Fig. 4) reveal a clear compositional dependence in the spatial distribution of lipid chains. DPPC exhibits a greater contribution to the central region of the bilayer compared to DLPC, indicating that its longer C16 acyl chains more frequently sample positions closer to the midplane. In contrast, the shorter C12 chains of DLPC remain more confined to their respective leaflets and contribute less to the bilayer center. This asymmetry reflects the underlying hydrophobic mismatch between the two lipid species.

Importantly, the increased DPPC density near the midplane should not be interpreted as uniform interdigitation. Instead, it reflects a broader distribution of chain conformations enabled by the greater length and flexibility of DPPC acyl chains. As the membrane becomes thinner and less densely packed, these chains can access central regions more readily. This behavior is consistent with hydrophobic mismatch, which is accommodated through conformational adjustment and local packing rearrangement rather than uniform penetration across leaflets [4, 5, 7].

The electron density profiles for the equimolar system (π = 0.50) further highlight this compositional asymmetry. After normalization, the peak electron densities are 160 for DPPC and 141 for DLPC, consistent with their molecular compositions. In the

bilayer center, DLPC exhibits a pronounced density minimum, whereas DPPC maintains a comparatively elevated density. This indicates that DPPC contributes more substantially to the central region, while DLPC remains largely excluded.

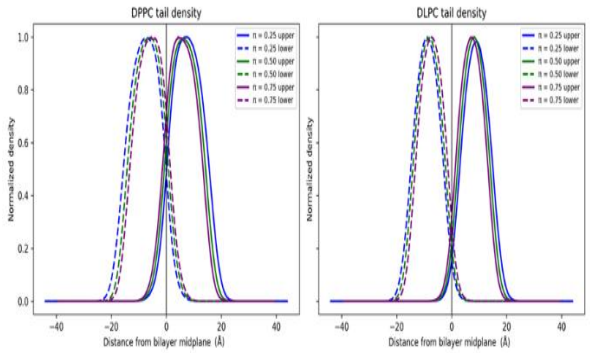

Fig. 4: Normalized tail mass density profiles of DPPC and DLPC along the bilayer normal

Together, the density profiles demonstrate that hydrophobic mismatch leads to a non-uniform spatial distribution of lipid species across the bilayer. The preferential central contribution from DPPC reflects structural adaptation to chain-length asymmetry, resulting in heterogeneous packing within the membrane interior. Similar features have been reported in experimental and simulation studies of asymmetric bilayer mixtures [4, 5, 7, 32].

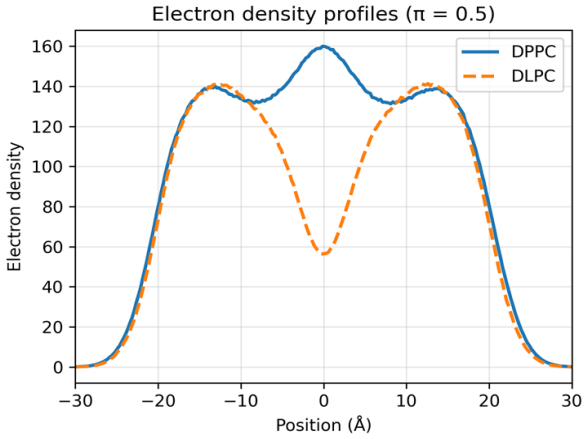

Fig. 5: Electron density profiles of DPPC/DLPC bilayers along the bilayer normal

3.3. Interleaflet Coupling Analysis

Interleaflet coupling in the mixed DPPC/DLPC bilayers was quantified using the chain overlap coefficient ($d_{overlap}$), which relates the effective chain extension along the bilayer normal to the hydrophobic core thickness. This parameter provides a measure of how closely lipid chains from opposing leaflets approach one another within the bilayer interior, with larger values indicating stronger interleaflet coupling.

The compositional dependence of $d_{overlap}$ is shown in Fig. 6. At low DLPC fraction (π = 0.25), the overlap values are relatively small (0.498 ± 0.050 for DPPC and 0.594 ± 0.089 for DLPC), indicating that lipid chains remain largely confined within their respective leaflets with limited interaction across the bilayer center.

At intermediate composition (π = 0.50), $d_{overlap}$ increases to 0.739 ± 0.066 for DPPC and 0.760 ± 0.058 for DLPC, reflecting a clear enhancement of interleaflet coupling. This trend continues at π = 0.75, where the values reach 0.933 ± 0.082 (DPPC) and 0.961 ± 0.040 (DLPC). Although these values approach unity, they remain below 1, indicating that the system does not exhibit fully interdigitated structures but rather a regime of strong interleaflet interaction.

The increase in $d_{overlap}$ with DLPC content arises primarily from the reduction in bilayer thickness, which decreases the separation between opposing leaflets and facilitates closer approach of lipid chains. As a result, interleaflet coupling strengthens progressively with increasing chain-length mismatch. Notably, the overlap values for DPPC and DLPC remain comparable across all compositions, suggesting that interleaflet coupling is a collective property of the bilayer rather than being dominated by a single lipid species. This behavior is consistent with the density profiles in Section 3.2, which show contributions from both lipids in the central region despite differences in chain length.

Overall, these results indicate that hydrophobic mismatch is accommodated through a continuous increase in interleaflet coupling driven by bilayer thinning and structural rearrangement. Rather than forming uniformly interdigitated configurations, the membrane adopts a state in which opposing chains approach closely within the bilayer core, contributing to the heterogeneous structural and dynamical behavior observed in subsequent sections.

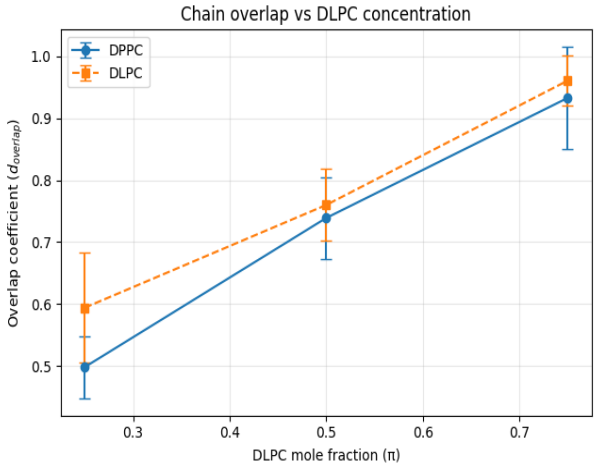

Fig. 6: Chain overlap coefficient as a function of DLPC mole fraction

3.4. Acyl Chain Order Parameters

The conformational ordering of lipid acyl chains was quantified using the deuterium order parameter $|S_{CD}|$ for both DPPC and DLPC at different compositions. As shown in Fig. 7, the order parameter profiles display the characteristic decrease along the acyl chain from the headgroup region toward the terminal methyl groups. This trend reflects the progressive increase in conformational freedom

toward the bilayer center, where chains experience fewer packing constraints.

A clear compositional dependence is observed for both lipid species. Increasing DLPC fraction (π) leads to a systematic reduction in chain ordering across the entire profile. The DLPC-rich system (25:75 DPPC:DLPC) exhibits the lowest $|S_{CD}|$ values, indicating increased conformational flexibility and reduced packing constraints within the hydrophobic core.

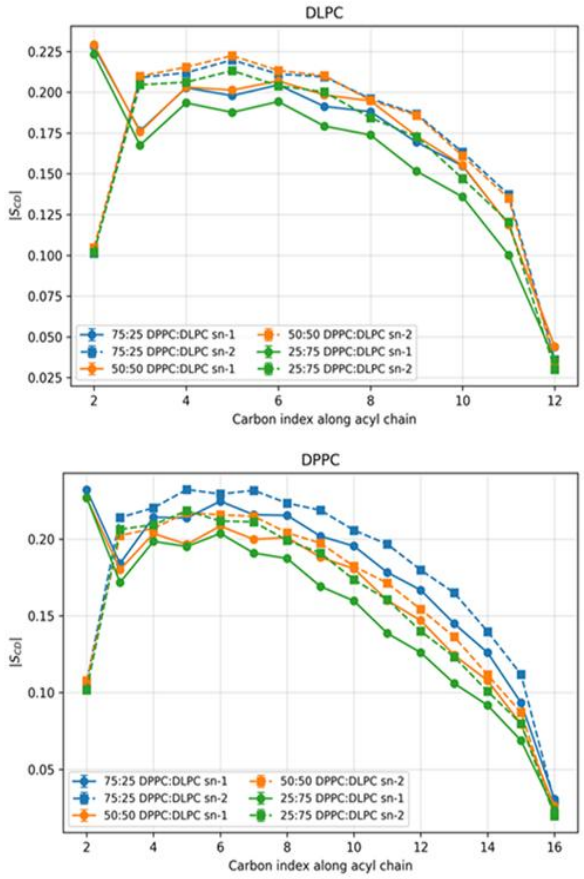

Fig. 7: Deuterium order parameter $|S_{CD}|$ profiles of DPPC and DLPC acyl chains (sn-1 and sn-2)

For DPPC, which possesses longer C16 chains, the reduction in ordering with increasing DLPC content is particularly pronounced in the mid-chain region. This region is most sensitive to packing disruptions, as it lies between the relatively constrained headgroup region and the highly flexible terminal segments. The presence of shorter DLPC chains introduces local packing mismatch, which perturbs the alignment of neighboring DPPC chains and promotes increased configurational freedom. A similar decrease in the order parameter of the longer lipid component upon addition of shorter lipid has been reported in mixed bilayers, supporting the interpretation that hydrophobic mismatch induces chain disordering [4].

For DLPC, the overall order parameter values remain lower than those of DPPC due to the shorter chain length and reduced van der Waals interactions. However, DLPC also exhibits a gradual decrease in ordering with increasing concentration, reflecting the collective nature of packing in mixed membranes. This indicates that even the shorter lipid species is influenced by the evolving membrane environment rather than behaving independently.

In agreement with previous experimental and simulation studies of mixed bilayers, the sn-2 chains consistently exhibit slightly higher ordering than the corresponding sn-1 chains, although the difference remains modest [18, 28]. This asymmetry arises from differences in chain geometry and packing constraints within the glycerol backbone region.

Importantly, the observed reduction in chain order provides a molecular-level explanation for the structural trends discussed in Sections 3.1–3.3. Decreased ordering reduces the effective projection of acyl chains along the bilayer normal, contributing to bilayer thinning and increased interleaflet coupling. At the same time, enhanced conformational flexibility increases lateral free volume, which is expected to facilitate lipid mobility and influence transport behavior.

Overall, these results demonstrate that increasing DLPC fraction progressively disrupts chain packing in both lipid species, leading to a more disordered and heterogeneous membrane structure. This disorder plays a central role in governing the dynamical and hydration properties of the bilayer, as discussed in the following sections.

3.5. Lateral Diffusion and Anomalous Transport

The lateral mobility of lipids in the DPPC/DLPC bilayers was analyzed using the mean squared displacement (MSD) and the corresponding diffusion coefficients (Fig. 8), together with log–log MSD analysis to assess anomalous transport behavior (Fig. 9).

The diffusion coefficients show a clear dependence on composition. At low DLPC fraction (π = 0.25), both lipid species exhibit similar mobilities, with D = (4.27 ± 1.7) × 10^{-7} cm^2/s for DPPC and (4.22 ± 1.8) × 10^{-7} cm^2/s for DLPC. At π = 0.50, mobility increases for both species, reaching (4.91 ± 1.9) × 10^{-7} cm^2/s for DPPC and (5.36 ± 1.0) × 10^{-7} cm^2/s for DLPC. At higher DLPC content (π = 0.75), the behavior diverges: DLPC continues to increase to (5.63 ± 0.78) × 10^{-7} cm^2/s, whereas DPPC decreases to (3.94 ± 1.7) × 10^{-7} cm^2/s.

The increase in DLPC mobility with composition is consistent with its shorter acyl chains, which reduce van der Waals interactions and lower membrane viscosity, facilitating lateral motion. In contrast, DPPC exhibits a weaker and non-monotonic dependence on composition, with a modest maximum near π = 0.50 followed by a decrease at higher DLPC fraction. The diffusion values obtained for DPPC are somewhat higher than those typically reported for fluid-phase bilayers in simulations and experiments (≈ 1.5 × 10^{-7} – 3 × 10^{-7} cm^2/s, depending on conditions) [33, 34]. This deviation is likely attributable to the elevated temperature (50 °C), enhanced membrane disorder, and the presence of shorter DLPC lipids, which reduce packing constraints and increase free volume, thereby facilitating faster lipid motion.

Despite these increases in diffusion coefficients, the log–log MSD analysis reveals that lipid motion remains subdiffusive across all compositions (Fig. 9).

The diffusion exponent α in Table 1 ranges from approximately 0.30 to 0.35 for both lipid species, significantly below the Fickian limit (α = 1). This indicates that lipid transport is governed by transient confinement and spatial heterogeneity rather than simple Brownian motion. A slight increase in α is observed at π = 0.50 (α ≈ 0.346–0.347), suggesting partial relaxation of constraints in the equimolar mixture, but no further increase occurs at higher DLPC content.

These results demonstrate that increased membrane fluidity does not lead to purely diffusive behavior. Instead, the system exhibits a regime of faster yet constrained motion, where enhanced mobility coexists with persistent subdiffusion. This behavior can be understood in terms of the structural changes described in earlier sections. Bilayer thinning, reduced chain order, and increased interleaflet coupling contribute to greater free volume and facilitate lipid displacement. At the same time, chain-length mismatch introduces local packing heterogeneity, which generates transient confinement and limits long-time diffusion.

The contrasting responses of DPPC and DLPC further highlight the role of molecular asymmetry. DLPC benefits directly from reduced packing constraints and shows a steady increase in mobility, whereas DPPC experiences competing effects: while increased free volume promotes motion, heterogeneous packing and mismatch-induced constraints reduce its mobility at high DLPC content.

Overall, lipid transport in DPPC/DLPC bilayers cannot be described solely by conventional diffusion coefficients. The coexistence of enhanced mobility and persistent subdiffusion indicates that membrane dynamics are controlled by the interplay between structural disorder, interleaflet coupling, and heterogeneous packing at the molecular scale.

3.6. Water Penetration Behavior

The water density profiles in Fig. 10 exhibit the characteristic bilayer structure, with bulk water plateaus (~33 nm^{-3}) in the aqueous phase and a pronounced depletion within the hydrophobic core. Despite this overall exclusion of water from the membrane interior, a clear compositional dependence is observed. Increasing the DLPC mole fraction leads to a progressive rise in water content within the bilayer core region.

Although the water density at the bilayer midplane remains very low (~10^{-3} nm^{-3}), the integrated core water (Fig. 11) increases substantially from 0.3372 nm^{-2} at π = 0.25 to 0.5526 nm^{-2} at π = 0.50 and 0.9265 nm^{-2} at π = 0.75. This monotonic increase demonstrates that even small changes in local density translate into a significant increase in the total amount of water accommodated within the membrane interior.

The increase in core hydration can be directly linked to the structural changes discussed in previous sections. As DLPC content increases, the bilayer undergoes lateral expansion and thinning (Section 3.1), enhanced interleaflet coupling (Section 3.3), and reduced acyl-chain ordering (Section 3.4). These effects collectively reduce packing efficiency within the hydrophobic core and generate transient free volume. This free volume enables water molecules to intermittently access regions that are otherwise hydrophobic, leading to increased water accommodation without requiring the formation of stable pores. These findings are consistent with previous simulation and experimental studies [9, 10].

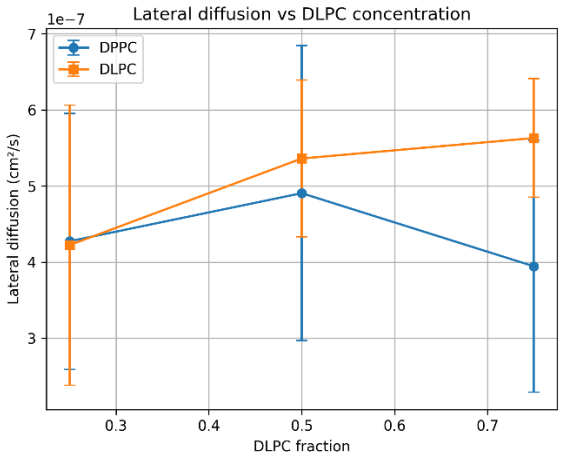

Fig. 8: Lateral diffusion coefficients of DPPC and DLPC as a function of DLPC mole fraction

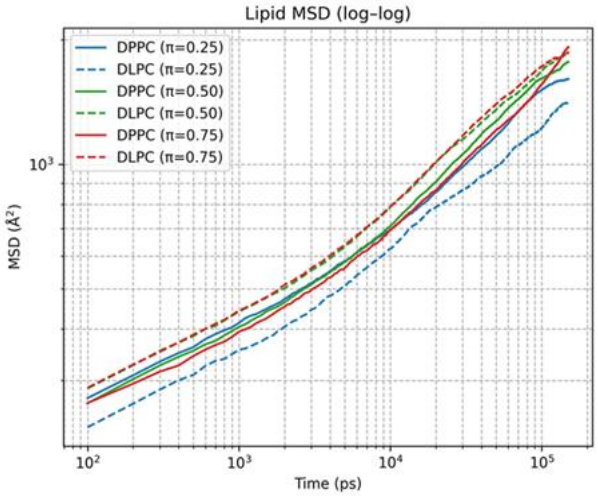

Fig. 9: Log–log MSD of DPPC and DLPC at different compositions

Table 1: Diffusion exponent (α) of DPPC and DLPC as a function of composition

π	α_DPPC	α_DLPC
0.25	0.299	0.305
0.50	0.347	0.346
0.75	0.327	0.350

Importantly, the density profiles show that the bilayer center remains a region of low water density, indicating that the membrane retains its integrity and does not undergo structural disruption. Instead, water molecules occupy transient, spatially heterogeneous regions associated with local packing fluctuations. This behavior is consistent with a dynamic picture in which water penetration is governed by short-lived defects rather than continuous channels.

When considered together with the diffusion and order parameter results (Sections 3.4–3.5), the present data indicate that DLPC enrichment leads to a membrane state characterized by increased mobility, reduced packing constraints, and enhanced structural heterogeneity. This combination promotes water accommodation within the bilayer interior while maintaining overall membrane integrity.

Overall, the results show that hydrophobic mismatch in DPPC/DLPC bilayers enhances membrane hydration through the creation of transient free volume and heterogeneous packing environments, rather than through the formation of permanent pores. This mechanism provides a direct link between molecular-level structural changes and membrane transport properties.

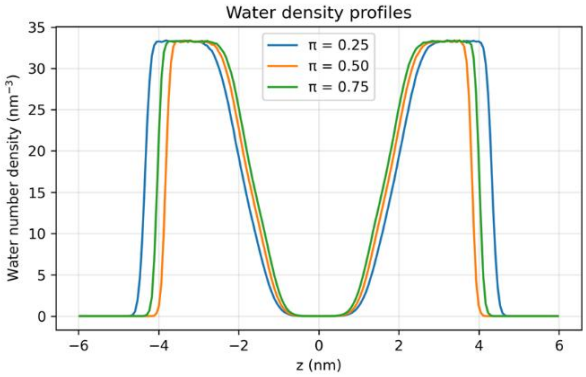

Fig. 10: Water oxygen number density profiles along the bilayer normal for DPPC/DLPC mixtures

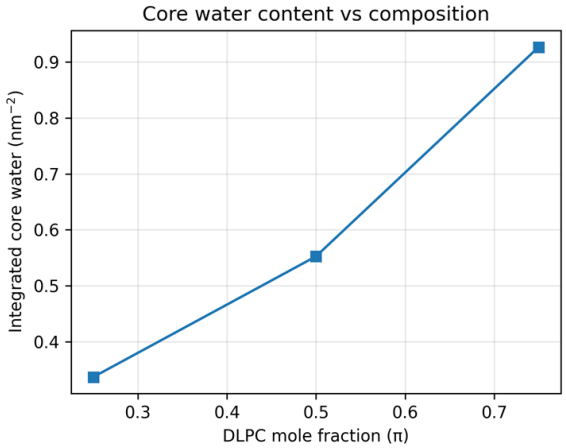

Fig. 11: Integrated core water as a function of DLPC mole fraction

4. Conclusions

This study provides a systematic atomistic investigation of the structural, dynamical, and hydration properties of mixed DPPC/DLPC bilayers, establishing a coherent molecular-level framework for understanding how moderate chain-length asymmetry governs membrane behavior.

Across all structural metrics, increasing DLPC fraction induces pronounced lateral expansion and bilayer thinning, reflecting reduced packing efficiency associated with the shorter C12 chains of DLPC. This structural reorganization is accompanied by a monotonic increase in interleaflet coupling, indicating that opposing lipid chains approach more closely as the bilayer thickness decreases. Importantly, the results show no evidence of fully developed interdigitation; instead, mismatch is accommodated through geometric adjustment and redistribution of chain conformations within the bilayer core.

At the molecular level, acyl-chain order parameters reveal a progressive reduction in chain ordering for both lipid species with increasing DLPC content, indicating enhanced conformational flexibility and disrupted packing. This structural disorder contributes directly to the observed changes in membrane thickness and interleaflet coupling, providing a consistent picture of mismatch accommodation.

The dynamical analysis demonstrates that lipid mobility exhibits composition-dependent behavior, with DLPC diffusion increasing steadily, while DPPC shows a non-monotonic trend with a maximum near the equimolar mixture. Despite these variations in diffusion coefficients, mean squared displacement analysis reveals persistent subdiffusive dynamics ($\alpha \approx 0.30–0.35$) across all compositions. This indicates that lipid motion remains governed by transient confinement and spatial heterogeneity, even in more fluid, DLPC-rich membranes.

Hydration analysis further shows that water content within the bilayer core increases significantly with DLPC fraction. This enhanced hydration arises from increased free volume and transient packing defects associated with bilayer thinning and reduced chain order, rather than from the formation of stable pores. The membrane therefore maintains structural integrity while becoming progressively more permeable at the molecular scale.

Taken together, these results demonstrate that hydrophobic mismatch in DPPC/DLPC bilayers is accommodated through a coupled set of mechanisms, including bilayer thinning, increased interleaflet coupling, and enhanced structural disorder. Rather than being governed by a single dominant process, membrane behavior emerges from the interplay between geometric constraints, molecular packing, and dynamic heterogeneity.

These findings provide new insight into how moderate chain-length asymmetry modulates membrane structure, dynamics, and hydration, and highlight the importance of considering anomalous diffusion and heterogeneous packing in describing membrane transport. The results have direct implications for the rational design of lipid-based systems, where tuning chain-length composition can be used to control membrane permeability, stability, and drug delivery performance.

References

[1] S. J. Marrink, V. Corradi, P. C. T. Souza, H. I. Ingólfsson, D. P. Tieleman, and M. S. P. Sansom, "Computational modeling of realistic cell membranes," *Chem. Rev.* **119**, 6184–6226 (2019), doi: 10.1021/acs.chemrev.8b00460.

[2] R. Friedman, S. Khalid, C. Aponte-Santamaría, E. Arutyunova, M. Becker, K. J. Boyd, M.

Christensen, J. T. S. Coimbra, S. Concilio, C. Daday, F. J. van Eerden, P. A. Fernandes, F. Gräter, D. Hakobyan, A. Heuer, K. Karathanou, F. Keller, M. J. Lemieux, S. J. Marrink, E. R. May, A. Mazumdar, R. Naftalin, M. Pickholz, S. Piotto, P. Pohl, P. Quinn, M. J. Ramos, B. Schiøtt, D. Sengupta, L. Sessa, S. Vanni, T. Zeppelin, V. Zoni, A.-N. Bondar, and C. Domene, "Understanding conformational dynamics of complex lipid mixtures relevant to biology," *J. Membr. Biol.* **251**, 609–631 (2018), doi: 10.1007/s00232-018-0050-y.

[3] W. Ding, M. Palaiokostas, W. Wang, and M. Orsi, "Effects of lipid composition on bilayer membranes quantified by all-atom molecular dynamics," *J. Phys. Chem. B* **119**, 15263–15274 (2015), doi: 10.1021/acs.jpcb.5b06604.

[4] A. H. Poghosyan, H. H. Gharabekyan, and A. A. Shahinyan, "Molecular dynamics simulations of DMPC/DPPC mixed bilayers," *Int. J. Mod. Phys. C* **18**, 73–89 (2007), doi: 10.1142/S0129183107010267.

[5] P. S. Coppock and J. T. Kindt, "Atomistic simulations of mixed-lipid bilayers in gel and fluid phases," *Langmuir* **25**, 352–359 (2009), doi: 10.1021/la802712q.

[6] B. Y. Wong and R. Faller, "Phase behavior and dynamic heterogeneities in lipids: a coarse-grained simulation study of DPPC-DPPE mixtures," *Biochim. Biophys. Acta Biomembr.* **1768**, 620–627 (2007), doi: 10.1016/j.bbamem.2006.12.009.

[7] G. Illya, R. Lipowsky, and J. C. Shillcock, "Effect of chain length and asymmetry on material properties of bilayer membranes," *J. Chem. Phys.* **122**, 244901 (2005), doi: 10.1063/1.1917794.

[8] J. Xu, V. Karra, D. E. Large, D. T. Auguste, and F. R. Hung, "Understanding the mechanical properties of ultradeformable liposomes using molecular dynamics simulations," *J. Phys. Chem. B* **127**, 9496–9512 (2023), doi: 10.1021/acs.jpcb.3c04386.

[9[R. M. Venable, A. Krämer, and R. W. Pastor, "Molecular dynamics simulations of membrane permeability," *Chem. Rev.* **119**, 5954–5997 (2019), doi: 10.1021/acs.chemrev.8b00486.

[10] J. Frallicciardi, J. Melcr, P. Siginou, S. J. Marrink, and B. Poolman, "Membrane thickness, lipid phase and sterol type are determining factors in the permeability of membranes to small solutes," *Nat. Commun.* **13**, 1605 (2022), doi: 10.1038/s41467-022-29272-x.

[11] I. T. Vattulainen and T. J. Róg, "Lipid membranes: theory and simulations bridged to experiments," *Biochim. Biophys. Acta Biomembr.* **1858**, 2251–2253 (2016), doi: 10.1016/j.bbamem.2016.06.007.

[12] H. Hashemzadeh, H. Javadi, and M. H. Darvishi, "Study of structural stability and formation mechanisms in DSPC and DPSM liposomes: a coarse-grained molecular dynamics simulation," *Sci. Rep.* **10**, 1837 (2020), doi: 10.1038/s41598-020-58730-z.

[13] G. Illya, "A diffusion-based model of doxorubicin release from liposomes: effects of size and membrane permeability," *Buletin Fisika* **26**, 222–230 (2025), doi: 10.24843/BF.2025.v26.i02.p09.

[14] S. Jo, T. Kim, V. G. Iyer, and W. Im, "CHARMM-GUI: a web-based graphical user interface for CHARMM," *J. Comput. Chem.* **29**, 1859–1865 (2008), doi: 10.1002/jcc.20945.

[15] B. R. Brooks, C. L. Brooks III, A. D. MacKerell Jr., L. Nilsson, R. J. Petrella, B. Roux, Y. Won, G. Archontis, C. Bartels, S. Boresch, A. Caflisch, L. Caves, Q. Cui, A. R. Dinner, M. Feig, S. Fischer, J. Gao, M. Hodoscek, W. Im, K. Kuczera, T. Lazaridis, J. Ma, V. Ovchinnikov, E. Paci, R. W. Pastor, C. B. Post, J. Z. Pu, M. Schaefer, B. Tidor, R. M. Venable, H. L. Woodcock, X. Wu, W. Yang, D. M. York, and M. Karplus, "CHARMM: the biomolecular simulation program," *J. Comput. Chem.* **30**, 1545–1614 (2009), doi: 10.1002/jcc.21287.

[16] J. Lee, X. Cheng, J. M. Swails, M. S. Yeom, P. K. Eastman, J. A. Lemkul, S. Wei, J. Buckner, J. C. Jeong, Y. Qi, S. Jo, V. S. Pande, D. A. Case, C. L. Brooks III, A. D. MacKerell Jr., J. B. Klauda, and W. Im, "CHARMM-GUI input generator for NAMD, GROMACS, AMBER, OpenMM, and CHARMM/OpenMM simulations using the CHARMM36 additive force field," *J. Chem. Theory Comput.* **12**, 405–413 (2016), doi: 10.1021/acs.jctc.5b00935.

[17] A. D. MacKerell Jr., D. Bashford, M. Bellott, R. L. Dunbrack Jr., J. D. Evanseck, M. J. Field, S. Fischer, J. Gao, H. Guo, S. Ha, D. Joseph-McCarthy, L. Kuchnir, K. Kuczera, F. T. K. Lau, C. Mattos, S. Michnick, T. Ngo, D. T. Nguyen, B. Prodhom, W. E. Reiher III, B. Roux, M. Schlenkrich, J. C. Smith, R. Stote, J. Straub, M. Watanabe, J. Wiórkiewicz-Kuczera, D. Yin, and M. Karplus, "All-atom empirical potential for molecular modeling and dynamics studies of proteins," *J. Phys. Chem. B* **102**, 3586–3616 (1998), doi: 10.1021/jp973084f.

[18] J. B. Klauda, R. M. Venable, J. A. Freites, J. W. O'Connor, D. J. Tobias, C. Mondragon-Ramirez, I. Vorobyov, A. D. MacKerell Jr., and R. W. Pastor, "Update of the CHARMM all-atom additive force field for lipids: validation on six lipid types," *J. Phys. Chem. B* **114**, 7830–7843 (2010), doi: 10.1021/jp101759q.

[19] R. W. Pastor and A. D. MacKerell Jr., "Development of the CHARMM force field for lipids," *J. Phys. Chem. Lett.* **2**, 1526–1532 (2011), doi: 10.1021/jz200167q.

[20[W. L. Jorgensen, J. Chandrasekhar, J. D. Madura, R. W. Impey, and M. L. Klein, "Comparison of simple potential functions for simulating liquid water," *J. Chem. Phys.* **79**, 926–935 (1983), doi: 10.1063/1.445869.

[21] M. J. Abraham, T. Murtola, R. Schulz, S. Páll, J. C. Smith, B. Hess, and E. Lindahl, "GROMACS: high performance molecular simulations through

multi-level parallelism from laptops to supercomputers," SoftwareX 1–2, 19–25 (2015), doi: 10.1016/j.softx.2015.06.001.

[22] D. van der Spoel, E. Lindahl, B. Hess, G. Groenhof, A. E. Mark, and H. J. C. Berendsen, "GROMACS: fast, flexible, and free," *J. Comput. Chem.* **26**, 1701–1718 (2005), doi: 10.1002/jcc.20291.

[23] S. Pronk, S. Páll, R. Schulz, P. Larsson, P. Bjelkmar, R. Apostolov, M. R. Shirts, J. C. Smith, P. M. Kasson, D. van der Spoel, B. Hess, and E. Lindahl, "GROMACS 4.5: a high-throughput and highly parallel open source molecular simulation toolkit," *Bioinformatics* **29**, 845–854 (2013), doi: 10.1093/bioinformatics/btt055.

[24] G. Bussi, D. Donadio, and M. Parrinello, "Canonical sampling through velocity rescaling," *J. Chem. Phys.* **126**, 014101 (2007), doi: 10.1063/1.2408420.

[25] M. Parrinello and A. Rahman, "Polymorphic transitions in single crystals: a new molecular dynamics method," *J. Appl. Phys.* **52**, 7182–7190 (1981), doi: 10.1063/1.328693.

[26] U. Essmann, L. Perera, M. L. Berkowitz, T. Darden, H. Lee, and L. G. Pedersen, "A smooth particle mesh Ewald method," *J. Chem. Phys.* **103**, 8577–8593 (1995), doi: 10.1063/1.470117.

[27] B. Hess, H. Bekker, H. J. C. Berendsen, and J. G. E. M. Fraaije, "LINCS: a linear constraint solver for molecular simulations," *J. Comput. Chem.* **18**, 1463–1472 (1997), doi: 10.1002/(SICI)1096-987X(199709)18:12<1463::AID-JCC4>3.0.CO;2-H.

[28] J. F. Nagle and S. Tristram-Nagle, "Structure of lipid bilayers," *Biochim. Biophys. Acta* **1469**, 159–195 (2000), doi: 10.1016/S0304-4157(00)00016-2.

[29] J. F. Nagle and S. Tristram-Nagle, "Lipid bilayer structure," *Curr. Opin. Struct. Biol.* **10**, 474–480 (2000), doi: 10.1016/S0959-440X(00)00117-2.

[30] J. F. Nagle, R. Zhang, S. Tristram-Nagle, W. Sun, H. I. Petrache, and R. M. Suter, "X-ray structure determination of fully hydrated Lα phase dipalmitoylphosphatidylcholine bilayers," *Biophys. J.* **70**, 1419–1431 (1996), doi: 10.1016/S0006-3495(96)79701-1.

[31] N. Kučerka, M.-P. Nieh, and J. Katsaras, "Fluid phase lipid areas and bilayer thicknesses of commonly used phosphatidylcholines as a function of temperature," *Biochim. Biophys. Acta Biomembr.* **1808**, 2761–2771 (2011), doi: 10.1016/j.bbamem.2011.07.022.

[32] N. Kučerka, S. Tristram-Nagle, and J. F. Nagle, "Structure of fully hydrated fluid phase lipid bilayers with monounsaturated chains," *J. Membr. Biol.* **208**, 193–202 (2006), doi: 10.1007/s00232-005-7006-8.

[33] U. Essmann and M. L. Berkowitz, "Dynamical properties of phospholipid bilayers from computer simulation," *Biophys. J.* **76**, 2081–2089 (1999), doi: 10.1016/S0006-3495(99)77364-9.

[34] J. Repáková, J. M. Holopainen, M. R. Morrow, M. C. McDonald, P. Capková, and I. Vattulainen, "Influence of DPH on the structure and dynamics of a DPPC bilayer," *Biophys. J.* **88**, 3398–3410 (2005), doi: 10.1529/biophysj.104.055533.